Baroclinic Instability in the Denmark Strait Overflow[1,2]

PETER C. SMITH

Bedford Institute of Oceanography, Dartmouth, Nova Scotia, Canada

(Manuscript received 1 September 1975, in revised form 12 January 1976)

ABSTRACT

Current meter records and hydrographic data taken in the Denmark Strait overflow during a one-month experiment in August–September 1973 are analyzed. Mean conditions indicate that a strong, cold overflow current existed throughout the experiment. The most outstanding feature of the velocity and temperature spectra is a strong peak at a period of 1.8 days. These oscillations appear to amplify in the downstream direction and are highly correlated over the entire flow at the southern end of the Strait. Phase estimates indicate that velocity components are in quadrature, while the cross-stream perturbation heat flux acts to reduce the mean potential energy associated with the sloping isotherms.

To explain the low-frequency variability, a quasi-geostrophic two-layer model for channel flow with a sloping bottom is developed. Using measured values of shear and other physical parameters, the model is found to be unstable over a limited range of wavelengths and frequencies. The most unstable wave is 80 km long and has a period of 2.1 days in close agreement with peaks in the current meter spectra. Furthermore, phase differences measured across the stream are found to be consistent with the propagation in the direction of the mean flow.

The study concludes with a discussion of finite-amplitude aspects of the instabilities.

1. Introduction

The overflow of Norwegian sea water through the Denmark Strait is recognized as an important source of North Atlantic Deep Water (Lee and Ellett, 1967). Oceanographic observations in the vicinity of the Denmark Strait have consistently revealed strong, highly variable current velocities as well as large fluctuations in composition of the overflow. In his pioneering work, Cooper (1955) suggested that the variability he observes in hydrographic sections south of the Strait results from the intermittent passage of large boluses of cold Norwegian sea water through the Strait. Harvey (1961) observed the bottom temperature on the western slope of the Strait to drop from 2.5°C to 0.1°C in a period of 20 h and was able to trace the advancing front of cold bottom water at a speed between 0.55 and 1.4 kt to a direction of roughly 255T. Recent investigations by Mann (1969) and Worthington (1969) support the earlier observations. Worthington's (1969) records of temperature and velocity from a mooring near the eastern edge of the overflow current show a distinct bimodal distribution with water warmer than 4°C moving slowly northward and cold water ($T<4$°C) moving swiftly out of the Strait to the southwest. His attempt to correlate the cold outbursts with meteorological conditions over the Norwegian Sea was unsuccessful. Mann (1969) observed the thickness of the overflow layer to change from 20 to 240 m in a period of 24 h and attributes the variable composition of the overflow to intermittency and turbulent mixing.

In the summer of 1973, scientists from the Bedford Institute aboard CSS *Hudson* conducted an investigation of the Denmark Strait overflow as part of an international experiment known as Overflow '73. The goal of the Canadian team was to measure the temporal and spatial variability of current velocity and water mass properties in and around the Denmark Strait for a period of one month. The purpose of the present study is to analyze and interpret the distinct low-frequency variability which was found in the records. The model developed is that of a uniform two-layer channel flow with a sloping bottom and has much in common with previous models for ocean and atmospheric circulations (Pedlosky, 1964; Orlanski, 1969; Blumsack and Gierasch, 1972). The stability of this system with respect to quasi-geostrophic disturbances will be investigated using mean conditions observed just south of the sill. The characteristics of the unstable baroclinic modes are then compared to the experimental data. The major difference between this and previous explanations of the overflow variability is that no upstream or meteorological forcing is required. Rather a steady flow of dense bottom water, driven by a constant upstream head in the Norwegian Sea, is intensified as it is funnelled through the Strait and becomes unstable hydrodynamically. As a result certain low-frequency fluctua-

[1] A Bedford Institute contribution.

[2] ICES Overflow 1973 Expedition Contribution No. 15.

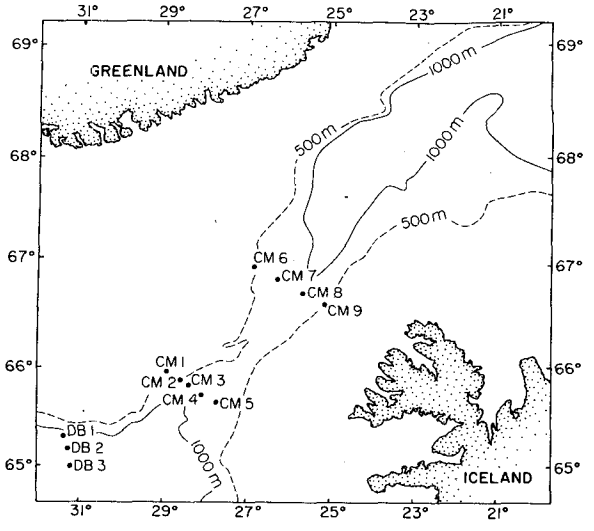

FIG. 1. Deployment of current meter moorings in the Denmark Strait.

tions are found in the overflow current at the southern end of the Strait.

A recent laboratory study of steady source flows in rotating systems (Smith, 1975) indicates that in a certain parameter range the finite-amplitude manifestation of these linear unstable waves is a continuous train of discrete vortices which propagate in the direction of the stream. On the other hand, analytical solutions for finite-amplitude baroclinic waves in a two-layer channel flow (Pedlosky, 1972) exhibit both spatial and temporal amplitude modulation in the form of wave packets which resemble solitary waves. Each of these separate results suggests that Cooper's boluses may indeed be the downstream signature of baroclinic instability in the Denmark Strait.

2. Overflow '73—The Denmark Strait experiment

The major Canadian contribution to the measurement program of Overflow '73 consisted of 12 moorings set in three lines across the axis of the flow as shown in Fig. 1. The moorings were instrumented with 26 Aanderaa current meters to record speed, direction and temperature every 15 min in the lower part of the water column with the deepest meters positioned 13 m above the bottom. The entire array was in place from 14 August to 15 September and the data return was excellent with the exception of CM5 which was lost (Ross, 1974). For this study, attention will be focused on results from the "southern" (CM1–CM4) and "northern" (CM6–CM9) current meter lines on either side of the controlling sill whose depth is 600 m. Individual meters will be referred to by a two-number code indicating mooring and depth respectively; for example (2,518) refers to the meter at a depth of 518 m on mooring CM2.

While the moorings were in place, dense and repeated hydrographic surveys were conducted in the Denmark Strait area. Representative temperature sections run near the northern and southern mooring lines are shown in Fig. 2. The locations of the current meters are indicated by black dots, but their relation to the bottom is distorted slightly due to depth variations between the mooring and section lines.

North of the sill the warm Atlantic water found at the surface on the eastern side of the Strait forms part of the Irminger Current which flows north around Iceland. On the western side, subzero temperatures mark the cold, fresh water of the East Greenland Current which flows southward along the Greenland continental shelf. Below the surface currents (below 300 m) lies a layer of Arctic Intermediate Water with temperatures and salinities between 0 and 1°C and 34.5 and 34.95‰, respectively. The subzero water in the deepest part of the section is identified as Norwegian Deep Water. These water mass designations and their locations within the section are the same as those of Mann (1969).

At the southern end of the Strait, the overflow water is distinguished by temperatures less than 2°C which are found along the bottom on the western side of the channel. A strong temperature contrast marks the boundary between the overflow and the warm Atlantic water above it. Again the subzero temperatures near the surface on the extreme western side identify the East Greenland Current. As Mann (1969) pointed out, it is difficult to trace individual water masses through the Strait in detail due to turbulent mixing and entrainment within the Strait itself.

Fig. 3 shows the σ_t sections corresponding to the temperature sections of Fig. 2. Superimposed on the density field are the average velocity vectors for the whole experiment at all current meters. The velocity component normal to each section line is plotted on the vertical axis at each meter with "down" implying toward the Atlantic Ocean. The northern section shows a large mass of dense water in the center of the channel but the current meters indicate small mean velocities. The most significant velocities occur near the edges of the Strait. On the western side, the isosteres near the bottom bend upward to follow the bottom slope and southward velocities of 12.3 and 16.1 cm s^{-1} are observed at CM6 mooring. On the eastern side, the isosteres slope strongly down to the bottom and the mean velocities at mooring CM9 show a current reversal with 7.8 cm s^{-1} northward at the upper meter and 21.7 cm s^{-1} southward at the bottom. Note that the density field and the sense of velocity shear are consistent with geostrophy.

At the southern line, the isosteres are densely packed near the bottom and are banked up against the western slope of the channel. The mean velocities are much stronger than at the northern line and are directed to the southwest except for the upper two sensors on

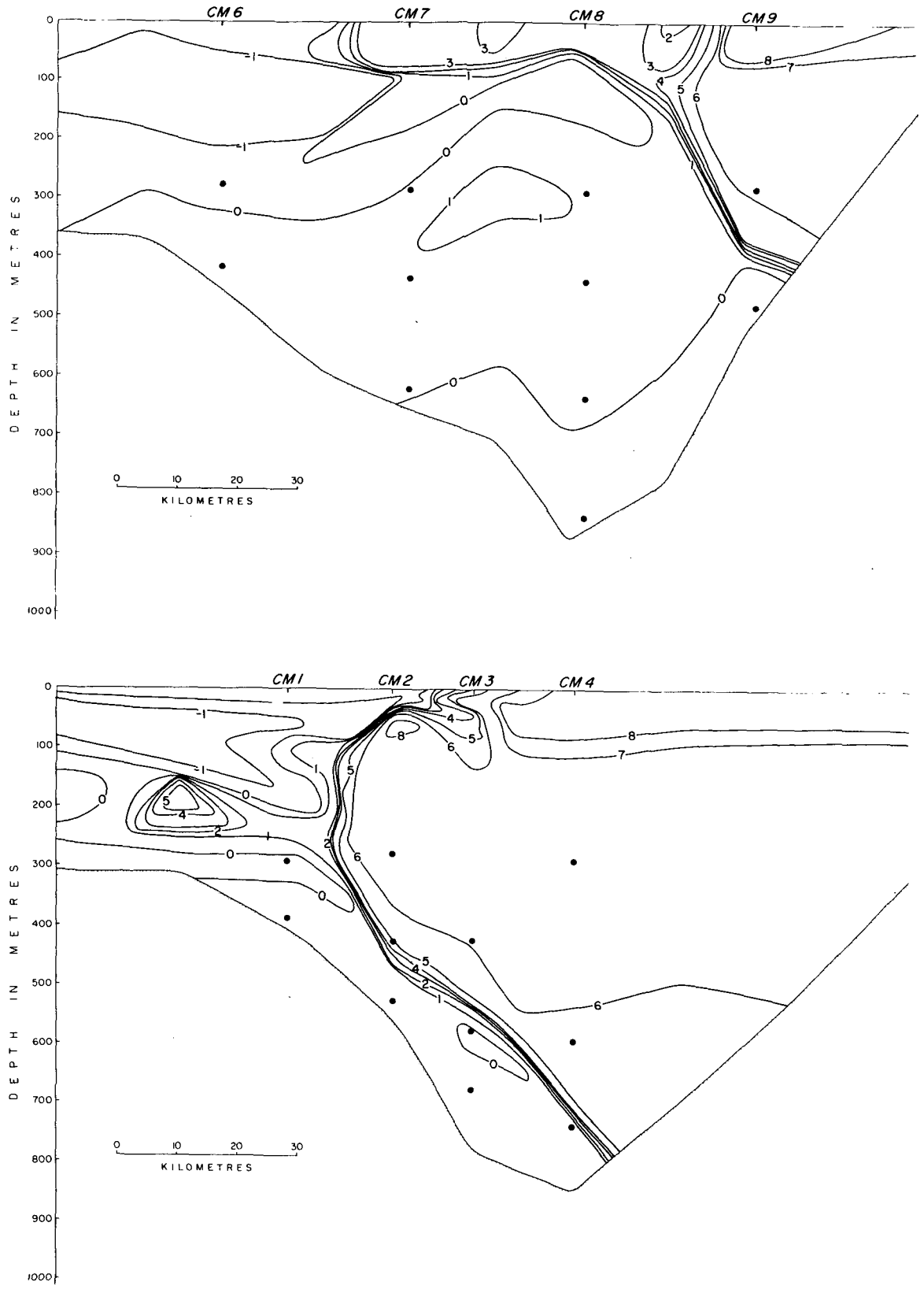

FIG. 2. Temperature sections from the Denmark Strait: (a) northern line (CM6–CM9), (b) southern line (CM1–CM4).

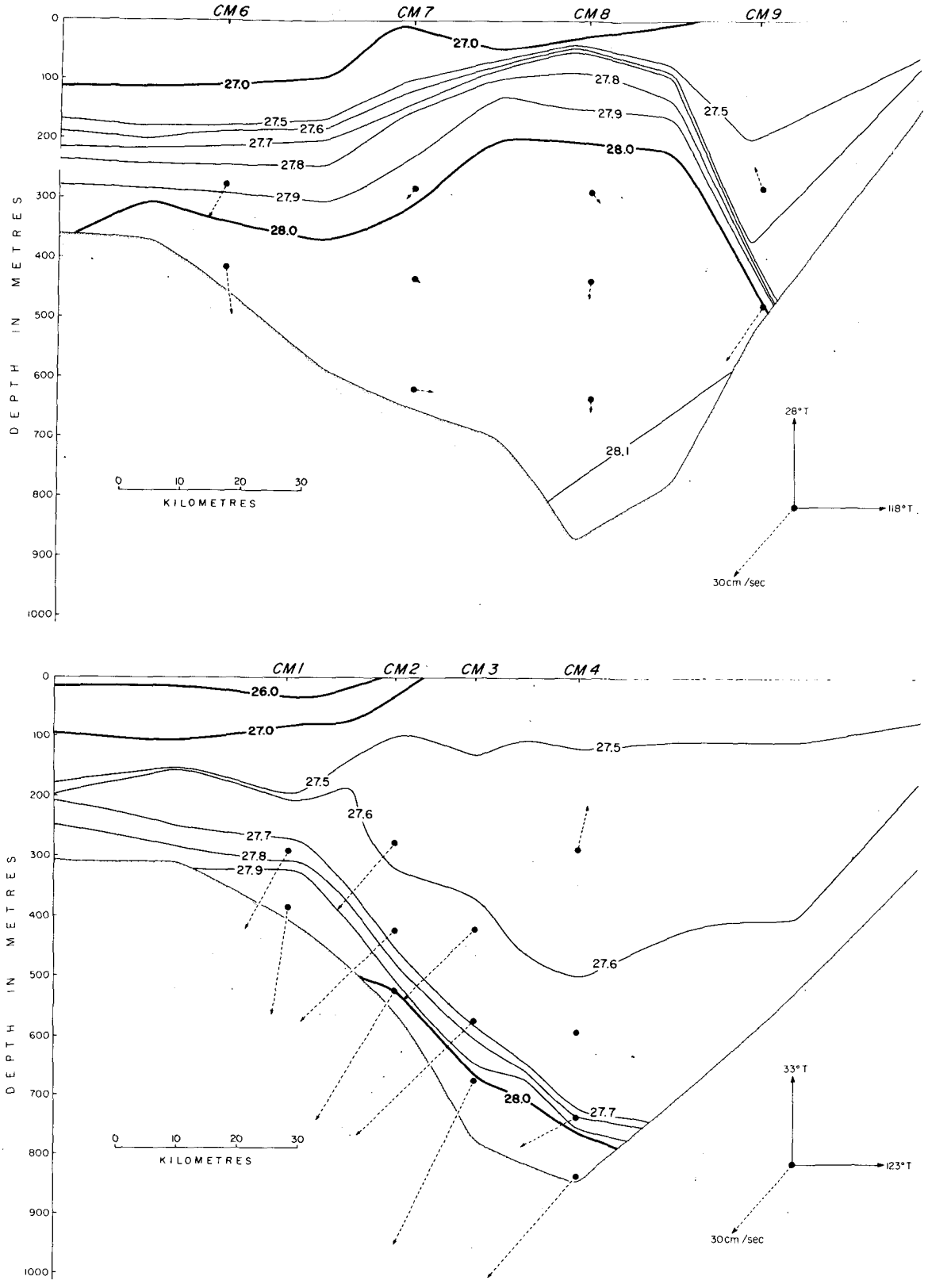

FIG. 3. Density sections from the Denmark Strait: (a) northern line, (b) southern line. Dashed lines are average current vectors at each meter.

CM4. The greatest velocities occur at the bottom meter on each mooring with the maximum of 60.1 cm s^{-1} at meter (3,665). Notice that water of the greatest density found at the southern section ($\sigma_t > 28.0$) is available from depths as shallow as 300 m at the northern line. Thus there exists a strong driving head for the overflow water at the north end of the Strait.

As noted earlier, the fields of temperature and density presented in Figs. 2 and 3 are not stationary. The profiles displayed in Fig. 4 give an indication of the variability observed near the CM3 mooring during the experiment. The STD stations from which the data are taken were separated by two weeks. In that time the position of the strong temperature and density contrast within the water column dropped 200 m and the average density of the overflow water decreased. According to Mann's (1969) observations, such changes may occur over 24 h.

Selected time series of temperature, speed and direction along with progressive vector diagrams from mooring CM3 are presented in Fig. 5. The temperature records indicate the presence of warm (6°C) water for a progressively larger percentage of time as the meter depth decreases. This pattern occurs consistently on all moorings in the southern line. The rate and direction records from the bottom meter on CM3 indicate that the onset of warm water is accompanied by a change in the current direction to the northwest quadrant. A detailed examination of the velocity and temperature records from all the bottom meters on the southern line has been given by Ross (1974). He finds that despite the evidence of warm spikes in each bottom temperature record, at no time were all four instruments simultaneously measuring temperatures in excess of 4°C.

The progressive vector plots indicate the strong mean component of the velocity field at all meters on CM3. The virtual displacements at the upper two meters are roughly colinear in the direction of 260T. The maximum displacement occurs at the bottom meter but its direction is rotated to 236T. Similar patters are evident at the other moorings in the southern line except CM4 where the upper two sensors show a weak net flow into the Norwegian Sea.

Superimposed on the mean current at the southern line is a distinct low-frequency variation which is evident in all records, especially the temperature records near the interface and the direction records at the bottom meters. A similar signal was present in Worthington's (1969) records of temperature and velocity from the eastern edge of the overflow at a depth of 761 m. The period of this oscillation as determined from the direction record in Fig. 5 is between 1.5 and 2 days. Before discussing the spectral characteristics of this low-frequency energy, the stability of the basic flow will be investigated using a simple channel flow model.

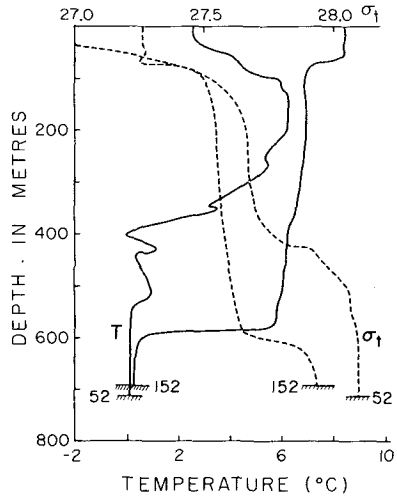

FIG. 4. Temperature and density profiles from the southern mooring line near CM3. STD stations (numbered sequentially) are separated by two weeks.

3. The model

From the data presented in the previous section, it is clear that a strong, highly variable overflow existed in the Denmark Strait throughout the Overflow '73 experiment. It is now possible to develop a simple model which exhibits the essential physical features of the baroclinic bottom current and investigate its stability. In a two-layer system, the flow in the bottom layer is driven by the upstream head in the Norwegian Sea and is assumed to be uniform and geostrophically balanced across the stream. As the dense water passes through the Strait, it is gradually set up against the western bank as the current intensifies. If the shear between the two layers exceeds a critical value, transition occurs and certain disturbances grow and propagate downstream. For a limited downstream range, the waves remain small, but as the perturbations amplify, nonlinear effects eventually become important. The extent of the linear regime depends on both the speed of propagation and growth rate of the unstable disturbances.

To simplify the stability analysis, the channel created by the Strait is assumed to have a uniform cross section, with a constant bottom slope α and vertical sides. The geometry of the basic flow field is shown in Fig. 6. The layer velocities are U_i ($i=1, 2$), the mean layer depths are D_i ($i=1, 2$) and the channel walls are at $y=\pm L/2$. The formulation of the linearized stability problem for quasi-geostrophic disturbances in a viscous bottom current on a beta plane is given in the Appendix. If the variables are normalized by lower layer quantities D_2, U_2, and the cross-stream scale L, then expansion for small Rossby number

$$\epsilon = \frac{U_2}{fL} \ll 1$$

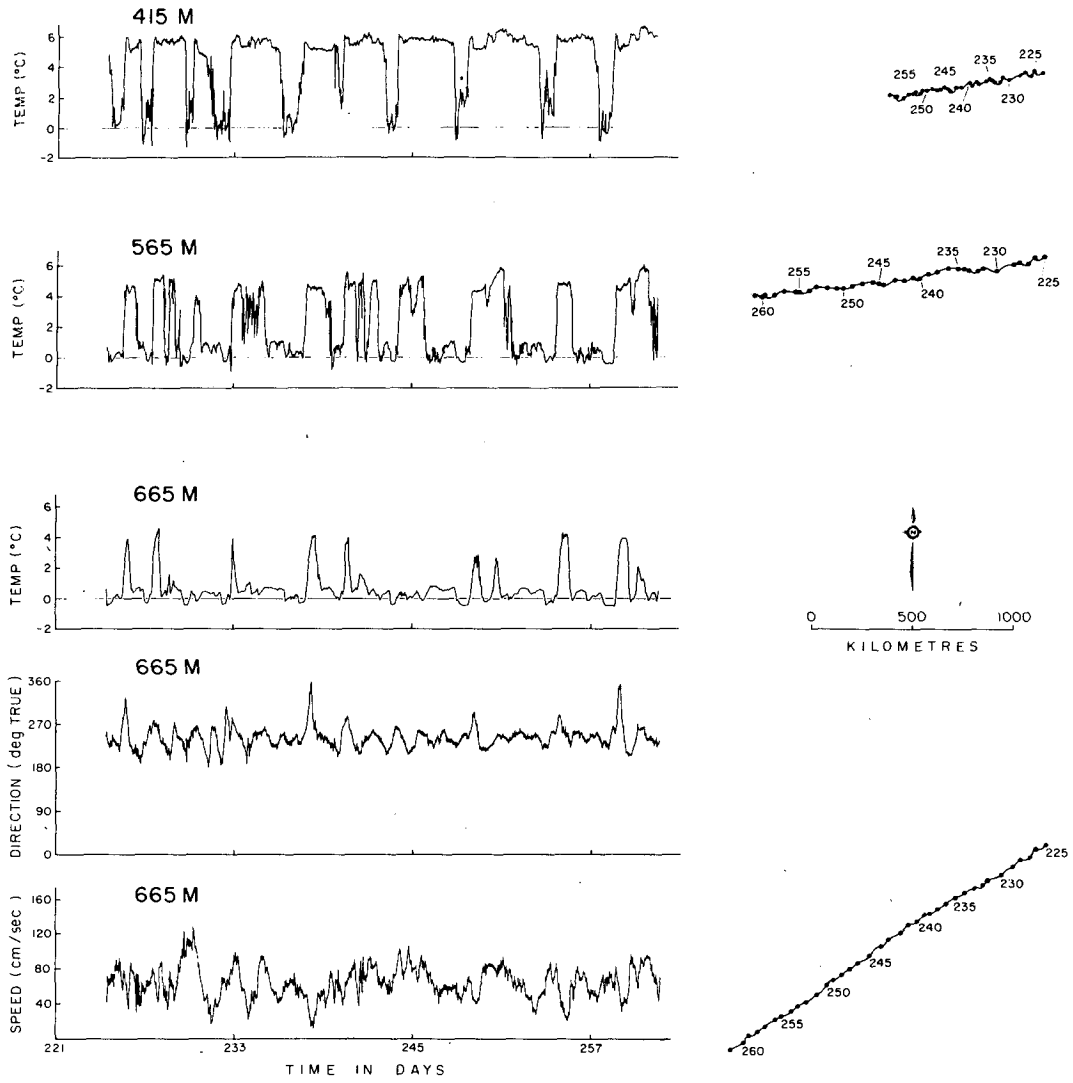

FIG. 5. Temperature, speed and direction records and progressive vector diagrams from CM3 current meter mooring.

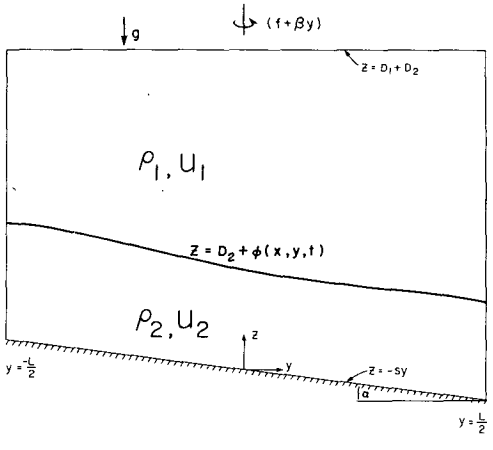

FIG. 6. Geometry of two-layer bottom current model.

yields coupled equations for the perturbation pressure fields:

$$\left(\frac{\partial}{\partial t}+U_1\frac{\partial}{\partial x}\right)[\nabla^2\psi_1+\gamma F(\psi_2-\psi_1)]$$

$$+F[\beta+\gamma(U_1-1)]\psi_{1x}=0, \tag{3.1}$$

$$\left(\frac{\partial}{\partial t}+\frac{\partial}{\partial x}\right)[\nabla^2\psi_2-F(\psi_2-\psi_1)]$$

$$+F[\beta-B-(U_1-1)]\psi_{2x}=-r\nabla^2\psi_2, \tag{3.2}$$

$$\nabla^2=\frac{\partial^2}{\partial x^2}+\frac{\partial^2}{\partial y^2},$$

with lateral boundary conditions

$$\frac{\partial \psi_i}{\partial x}=0, \qquad i=1, 2, \tag{3.3}$$

$$\lim_{x\to\infty}\frac{1}{2x}\int_{-x}^{x}\frac{\partial^2\psi_i}{\partial y\partial t}dx=0, \quad \text{at} \quad y=\pm\tfrac{1}{2}. \tag{3.4}$$

In addition to the Rossby number constraint, the parameters appearing in these equations are defined and restricted as follows:

$$\left.\begin{aligned} \mathrm{B}&=\frac{g_r s}{fU_2}\leqslant \mathrm{O}(\mathrm{F}^{-1}) & \mathrm{F}&=\frac{f^2L^2}{g_rD_2}\\ r&=\frac{\mathrm{E}^{\frac{1}{2}}}{2\epsilon}\leqslant \mathrm{O}(1) & \mathrm{E}&=\frac{\nu}{fD_2^2}\\ \beta&=\frac{g_rD_2}{fU_2}\left(\frac{\cot\theta}{R}\right)_y \end{aligned}\right\}, \tag{3.5}$$

where ν is the constant eddy viscosity, $g_r=(\Delta\rho/\rho_2)g$ is reduced gravity, and $(\cot\theta/R)_y$ is the y projection of the variation in Coriolis parameter.

The eigenfunctions for (3.1)–(3.4) are

$$\psi_1=\mathrm{Re}[\mu A e^{ik(x-ct)}\cos(m\pi y)], \tag{3.6}$$

$$\psi_2=\mathrm{Re}[A e^{ik(x-ct)}\cos(m\pi y)], \tag{3.7}$$

$m=1, 2, \ldots$, where k is the downstream wavenumber, A is the amplitude of the wave (both assumed real), $\mu=\mu_r+\mu_i$ is the complex amplitude ratio and $c=c_r+ic_i$ is the complex phase speed. Substitution into (3.1) and (3.2) gives a quadratic equation for the phase speed c:

$$ac^2+bc+d=0, \tag{3.8}$$

where

$$\left.\begin{aligned} a&=\alpha(\alpha+\gamma+1)\\ b&=q_1(\alpha+1)+q_2(\alpha+\gamma)-\alpha(U_1+1)(\alpha+\gamma+1)\\ d&=q_1q_2-q_1(\alpha+1)-U_1q_2(\alpha+\gamma)+U_1\alpha(\alpha+\gamma+1) \end{aligned}\right\}$$

and

$$\left.\begin{aligned} \alpha&=(k^2+m^2\pi^2)/\mathrm{F}\\ q_1&=\beta-\gamma(1-U_1)\\ q_2&=\beta-\mathrm{B}+(1-U_1)+i\frac{r\alpha}{k} \end{aligned}\right\}.$$

The solution to (3.8)

$$c=c_r+ic_i=-\frac{b}{2a}\pm\frac{1}{2a}[b^2-4ad]^{\frac{1}{2}}, \tag{3.9}$$

together with the expressions for the complex amplitude components

$$\mu_r=\alpha+1+\frac{[\beta-\mathrm{B}+(1-U_1)](c_r-1)+\frac{r\alpha}{k}c_i}{|c-1|^2}, \tag{3.10}$$

$$\mu_i=\frac{\frac{r\alpha}{k}(c_r-1)-[\beta-\mathrm{B}+(1-U_1)]c_i}{|c-1|^2}, \tag{3.11}$$

where

$$|c-1|^2=(c_r-1)^2+c_i^2,$$

specify the complete solution to the linear stability problem.

The dependence of the eigenvalues $c(k,m;\beta,\mathrm{B},U_1,\gamma,\mathrm{F},r)$ on the external parameters of the system has been thoroughly studied in other contexts. Therefore only a few of the salient features will be brought out by considering an example with typical conditions observed at the southern current meter line in the Denmark Strait (see Table 1). For simplicity, the flow is assumed inviscid with the upper layer at rest ($r=U_1=0$). Calculations of the dispersion characteristics for the mode 1 ($m=1$) instabilities are displayed in Fig. 7. In this case, $\mathrm{B}^{-1}=fU_2/(g_rs)$, a dimensionless measure of the lower layer velocity and the shear at the interface, has been plotted against wavelength. The inviscid flow is unstable for $\mathrm{B}^{-1}\geqslant 1$, which implies that the shear is greater than the geostrophic velocity based on the

TABLE 1. Physical constants and dimensionless parameters at the southern mooring line

Part 1.

Physical constant	Estimated value	Error	Units
D_1	400	±100	m
D_2	150	± 50	m
L	100	± 30	km
g_r	0.45	± 0.05	cm s^{-2}
s	0.01	± 0.003	
f	1.3×10^{-4}		s^{-1}
β	-0.5×10^{-13}		cm^{-1} s^{-1}
ν	0	+ 10	cm^2 s^{-1}
U_1	0	− 10	cm s^{-1}
U_2	60	± 10	cm s^{-1}

Part 2.

Dimensionless	Value	Error
$\mathrm{F}[=f^2L^2/g_rD_2]$	250	±100
$\mathrm{B}[=g_rs/fU_2]$	0.346	±0.040
$U_1[=U_1/U_2]$	0	−0.2
$\gamma[=D_2/D_1]$	0.375	±0.175
$\epsilon[=U_2/fL]$	0.05	±0.03
$\mathrm{E}[=\nu/fD_2^2]$	0	+0.0003
$r[=\mathrm{E}^{\frac{1}{2}}/2\epsilon]$	0	+0.2

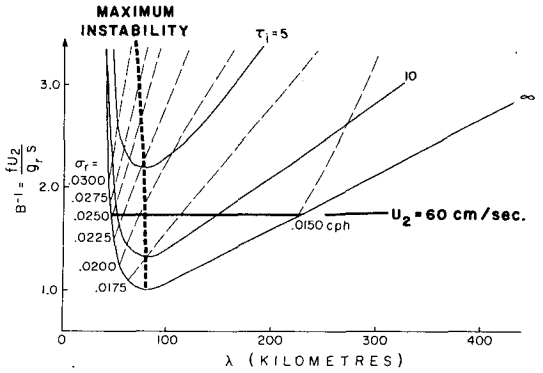

FIG. 7. Stability diagram for mode 1 channel flow instabilities in the Denmark Strait. Parameters used are the nominal values in Table 1.

slope $g_r s/f$, or equivalently the interface slope exceeds the bottom slope. This criterion corresponds to Pedlosky's (1964) necessary condition for instability and is shown by these calculations to be a sufficient condition also. For an estimated bottom velocity of 60 cm s^{-1}, the value of B^{-1} corresponds to a finite range of instabilities. The growth rates are given inversely in terms of $\tau_i = f/(kc_i)$, which represents the number of inertial periods required for the wave amplitude to e-fold. The real frequencies $\sigma_r = kc_r$ for the unstable waves (expressed in cycles per hour) are subtidal and the wavelengths $\lambda = 2\pi L/k$ are centered around 80 km. The wavelength of the maximally unstable wave changes little over the range of the shear parameter considered $[1 \leqslant fU_2/(g_r s) \leqslant 3]$. Hence the primary effect of increasing U_2 is to increase the frequency σ_r and enhance the growth rate.

Several other remarks about the model are pertinent.

1) The presence of a negative velocity ($U_1 < 0$) in the upper layer produces no significant change in wavelength of the most unstable wave, but reduces its frequency and increases the growth rate due to the enhanced shear. For $U_2 = -0.2$, reductions in both σ_r and τ_i amount to roughly 20%.

2) For small values of r ($\leqslant 0.5$), unstable waves exist for $B^{-1} < 1$ and extend over the entire range of wavelengths. However, the growth rates of these purely viscous waves are more than an order of magnitude lower than those of the maximum instability. Furthermore, viscosity has no measurable effect on the frequency and wavelength of the most unstable wave and its growth rate is diminished by less than 5%.

3) The influence of the planetary vorticity gradient (β effect) is totally masked by topographic effects in this parameter range. This result is anticipated from the scaling since $\beta/B = O(10^{-2})$. The magnitude of ϵFB (4.0, for this example) is order 1 not ϵ indicating that the assumption of small slope may not be valid. However, the expression for the vertical velocity induced by the bottom slope contains the cross-stream velocity component which is scaled by U_2. Since the basic geostrophic flow follows bottom contours, the cross-stream velocities are overestimated by U_2. Hence the vertical velocities are small in spite of the strong bottom slope.

4) With other parameters fixed, the first cross-stream mode instabilities ($m = 1$) have the largest growth rate. For this example, the difference in τ_i is 27% between the first and second modes and 104% between first and third for the most unstable wave.

A derivation of the energy transformations for a more general two-layer model including horizontal shear in each layer is also presented in the Appendix. The equation governing the time rate-of-change of perturbation energy [Eq. (A29)], in dimensional form and neglecting dissipation, may be written as

$$\frac{1}{2}\frac{\partial}{\partial t}(\rho_1 D_1 \overline{u_1'^2} + \rho_2 D_2 \overline{u_2'^2} + \Delta\rho g \overline{\phi'^2}) = \rho_2 f \overline{(U_2 - U_1) v_2' \phi'}$$

$$- (\rho_1 D_1 \overline{U_{1y} u_1' v_1'} + \rho_2 D_2 \overline{U_{2y} u_2' v_2'}), \quad (3.12)$$

where the prime denotes a perturbation quantity and

$$\overline{(\quad)} = \frac{1}{\lambda}\int_{-L/2}^{L/2}\int_0^{\lambda} (\quad) dx dy.$$

The first term on the right-hand side of (3.12) represents the transfer of energy from the available potential energy of the mean flow into the perturbations. It is the essence of baroclinic instability. The other terms represent the transfer of energy between the mean flow kinetic energy and the perturbations. The approximation of uniform flow within each layer ($U_{iy} = 0$, $i = 1, 2$) in the present model eliminates the mean kinetic energy as a source of perturbation energy. Hence the instability must be purely baroclinic. According to the scaled energy transformations appearing in (A28), the ratio of baroclinic to barotropic transfer in the general model is F, the internal Froude number. Thus for the large values of F in the Denmark Strait the neglect of shear in U_i is justified. This conclusion is supported by the results of Hart (1974), who found no significant barotropic energy transfer for $F \geqslant 1$ in his calculations of the mixed stability problem for a shearing surface over flat topography.

The model results in Fig. 7 suggest that baroclinic instability is a possible source of low-frequency variability in the temperature and current meter records from Denmark Strait. In the next section, the nature of this variability will be examined in an attempt to confirm this hypothesis. To facilitate the comparison, certain dimensional forms are required. Expressions for the perturbation velocity components are determined from derivatives of the pressure perturbations

(3.6) and (3.7):

$$\left.\begin{aligned} u_2' &= \frac{m\pi A^*}{\rho_2 f L}\sin\left(\frac{m\pi y}{L}\right)\cos(kx-\sigma_r t)e^{\sigma_i t} \\ v_2' &= -\frac{kA^*}{\rho_2 f}\cos\left(\frac{m\pi y}{L}\right)\sin(kx-\sigma_r t)e^{\sigma_i t} \\ u_1' &= \frac{m\pi|\mu|A^*}{\rho_1 f L}\sin\left(\frac{m\pi y}{I}\right)\cos(kx-\sigma_r t+\delta)e^{\sigma_i t} \\ v_1' &= -\frac{k|\mu|A^*}{\rho_1 f L}\cos\left(\frac{m\pi y}{L}\right)\sin(kx-\sigma_r t+\delta)e^{\sigma_i t} \end{aligned}\right\}, \quad (3.13)$$

where $A^*=\rho_2 f U_2 L A$ is the magnitude of the original pressure perturbation and

$$|\mu|^2=\mu_r^2+\mu_i^2; \quad \tan\delta=\mu_i/\mu_r.$$

When the amplification rate is weak ($\sigma_i/\sigma_r \ll 1$) the downstream averaged perturbation kinetic energy components in the lower layer, given by

$$\left.\begin{aligned} \tfrac{1}{2}\rho_2 D_2\langle u_2'\rangle^2 &= \frac{m^2\pi^2 A^{*2} D_2}{4\rho_2 f^2 L^2}\sin^2\left(\frac{m\pi y}{L}\right)e^{2\sigma_i t} \\ \tfrac{1}{2}\rho_2 D_2\langle v_2'\rangle^2 &= \frac{k^2 A^{*2} D_2}{4\rho_2 f^2}\cos^2\left(\frac{m\pi y}{L}\right)e^{2\sigma_i t} \end{aligned}\right\}, \quad (3.14)$$

are equivalent to time averages over one wave period at a fixed point ($x=0$) for time t following the onset of instability.

4. Low-frequency variability in the Denmark Strait

The investigation of the low-frequency aspects of the Denmark Strait overflow is focused on data from the southern mooring line. Interpretation of these data is based on characteristics of the two-layer model instabilities for the parameter range given in Table 1. Physical constants at the southern line were estimated from a survey of all the current meter and hydrographic data taken there during the experiment with the exception of the eddy viscosity whose value is considered reasonable for currents of this scale (Smith, 1973). The corresponding constants for the northern section are somewhat different (e.g., lower velocities, weaker density contrasts) but the net effect on the maximum instability (lower frequencies, shorter wavelengths, smaller growth rates) is not detectable within the overall uncertainty of the measurements and will therefore be disregarded when referring to observations at the northern line. The primary function of the linearized stability analysis then is to provide a range of unstable frequencies, wavelengths, growth rates, and the associated phase relationships for solutions in the parameter range given in Table 1.

The direction of the mean velocity at the core of the overflow is estimated at roughly 250T based on the progressive vector displacements shown in Fig. 5. Therefore for purposes of spectral analysis, the velocity components will be resolved with respect to this direction, and downstream and cross-stream perturbations will refer to components at 250T and 160T, respectively.

a. The spectra

The standard spectral analysis package at the Bedford Institute (Dobson *et al.*, 1974) uses the fast Fourier transform technique to determine the spectral content of the velocity and temperature time series. The 15 min data were analyzed and filtered in K non-overlapping blocks (usually $K=7$) of 512 samples each and the spectral estimates were derived from averages of the Fourier coefficients over all blocks. At low frequencies the spectral estimates had roughly 15 degrees of freedom for which the 95% confidence limits are 0.55–2.4 times the value (Munk *et al.*, 1959). However, the standard deviation of spectral estimates among blocks, which includes non-stationarity as well as random errors, generally exceeds the 95% confidence limits. This indicates that the variability at these frequencies is intermittent. In the results which follow, the standard deviation of the low-frequency spectral peak is plotted as a measure of the total error.

The spectra of velocity and temperature at mooring CM3 are presented in Fig. 8. Estimates of frequency times the total velocity spectrum ($\Phi=\Phi_{uu}+\Phi_{vv}$), which is invariant under rotation, show a strong peak of low-frequency energy centered at $\sigma=0.0231$ cycle per hour (cph) [1.8-day period]. The kinetic energy content in this range is nearly the same for the upper two meters but is much lower at the bottom meter. This reduction is probably caused by attenuation of the velocity field by the bottom boundary layer. There is also a weaker but distinct peak near the semidiurnal tidal frequency $\sigma_{M_2}\approx 0.0805$ cph. The strength of temperature fluctuations at these meters increases with distance from the bottom as would be expected from the records of Fig. 5. The temperature peaks are associated with the heaving of the interface between the overflow and the 6°C Atlantic water; they correspond to the kinetic energy peak with the exception of (3,415). Note that the attenuation of the temperature variability with depth does not necessarily imply less vertical motion because the deeper water tends to be more homogeneous.

The distributions of spectral energy at the other moorings in the southern line are quite similar to that at CM3, and the magnitudes are comparable except for the upper meter on CM4 where the peaks are smaller by a factor of 5. A summary of the low-frequency kinetic energy content along lines parallel to the slope is presented in Fig. 9. The estimates for $\bar{\Phi}_{uu}$ and $\bar{\Phi}_{vv}$ were obtained by integrating the first four spectral

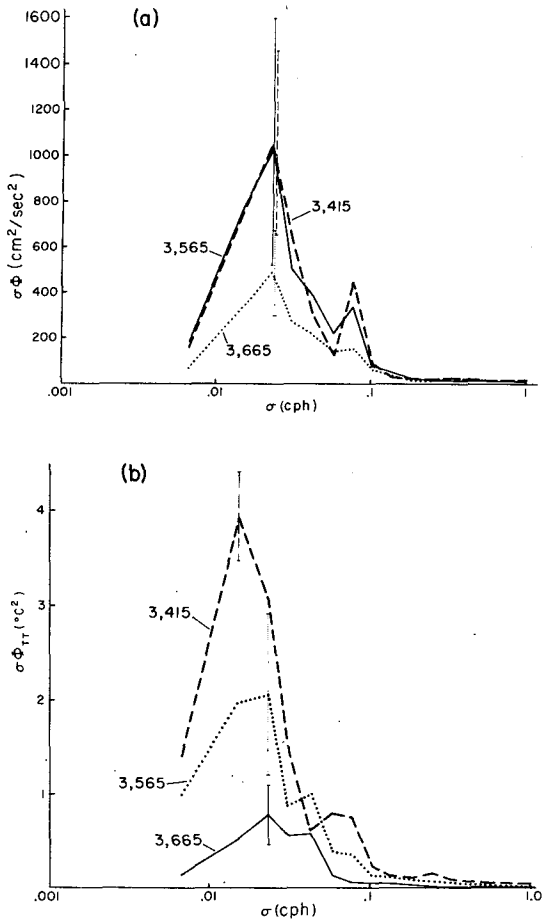

FIG. 8. Spectra of velocity and temperature at CM3: (a) frequency times total velocity spectrum [$\sigma\Phi=\sigma(\Phi_{uu}+\Phi_{vv})$], (b) frequency times temperature spectrum.

values over the frequency band $0<\sigma\leqslant 0.031$ cph, e.g.,

$$\bar{\Phi}_{uu}=\Delta\sigma\sum_{n=1}^{4}(\Phi_{uu})_n, \quad \Delta\sigma=0.00871 \text{ cph}.$$

According to the model, the relative energy in the average cross-stream and downstream velocity perturbations are distributed as $\cos^2(m\pi y/L)$ and $(m^2\pi^2/k^2)\times\sin^2(m\pi y/L)$ across the stream. These functions calculated for the maximum mode instability are plotted at the bottom of Fig. 9. As predicted, the cross-stream fluctuations reach a maximum in the center of the channel and there is some evidence for intensification of the downstream oscillations at the edges of the flow particularly at the bottom. However, the measured energy in the downstream component is much too large relative to that of the cross-stream component. Thus although the distribution of kinetic energy components is qualitatively the same as that of a first-mode linear wave, the partitioning of energy is distinctly different. This result may be related to finite-amplitude characteristics of the unstable waves as discussed in Section 5.

Unlike the records south of the sill, the measurements along the northern line showed very little spectral energy at low frequencies. With the exception of CM6, the northern moorings showed kinetic energy levels reduced by an order of magnitude from those at the southern line. At CM6, however, the bottom meter (6,418), showed a low-frequency peak in the velocity spectrum which is comparable to that observed at the bottom on CM2. These two spectra along with those from an upper sensor on each mooring are displayed in Fig. 10a. In contrast to the bottom records, the downstream amplification observed between the upper meters is striking. A gross measure of this amplification is presented in Fig. 10b where the average low-frequency kinetic energy level per sensor on each mooring in the northern line is compared with that at the

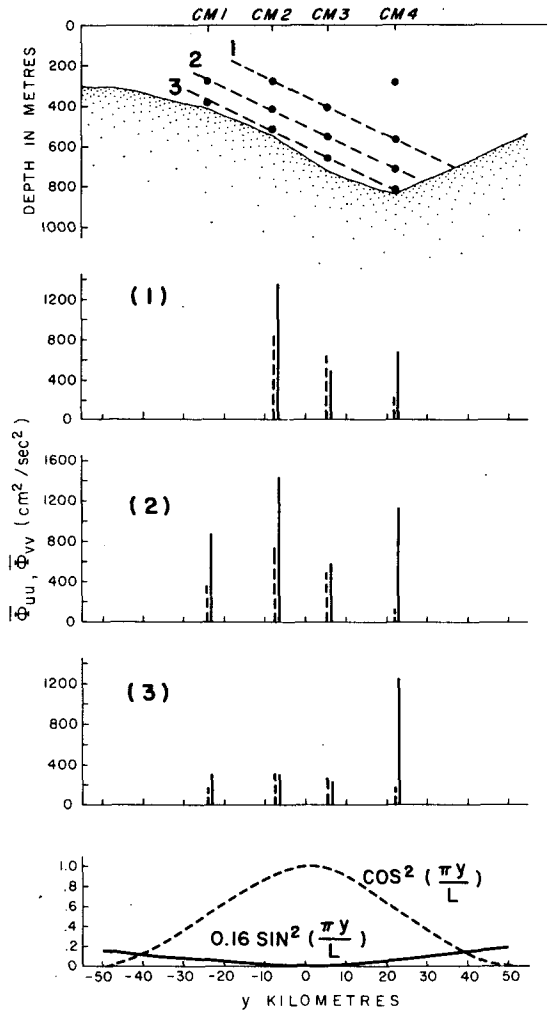

FIG. 9. Low-frequency kinetic energy content at southern mooring line for the downstream component $\bar{\Phi}_{uu}=\Delta\sigma\sum_{n=1}^{4}(\Phi_{uu})_n$, $\Delta\sigma=0.00781$ cph [solid lines], and the cross-stream component $\bar{\Phi}_{vv}=\Delta\sigma\sum_{n=1}^{4}(\Phi_{vv})_n$ [dashed lines].

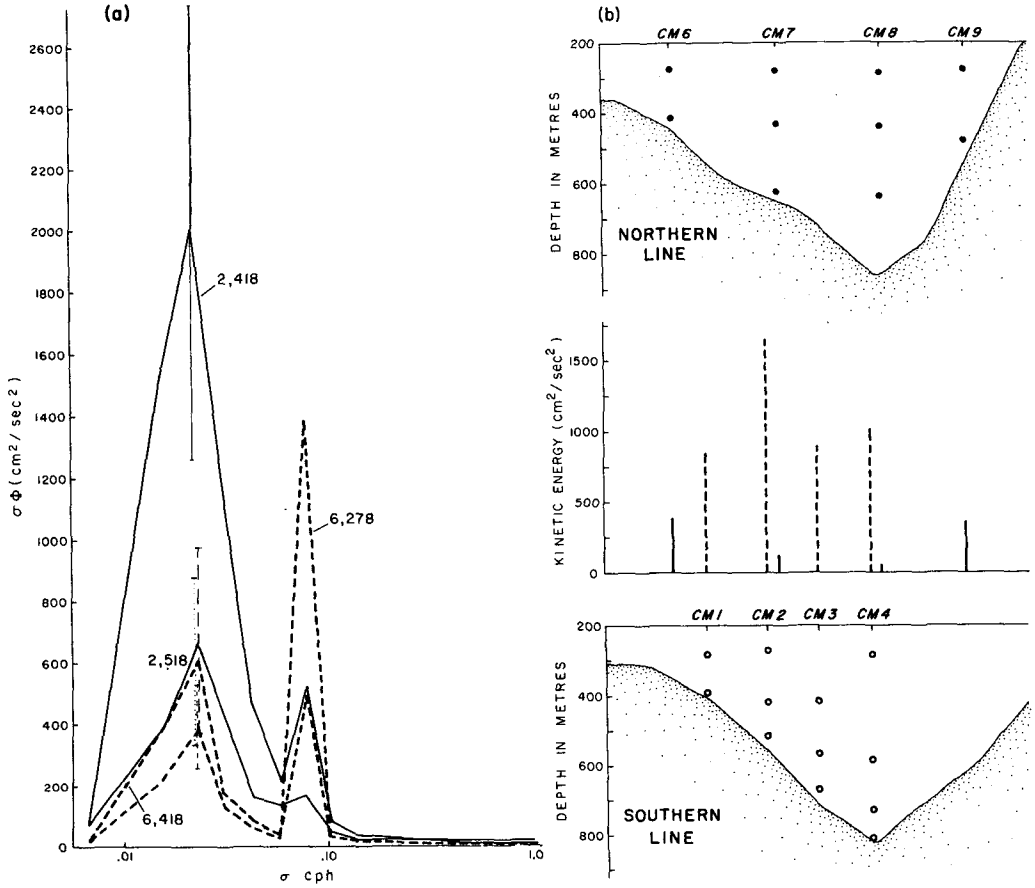

FIG. 10. Downstream amplification of low-frequency kinetic energy: (a) velocity spectra from northern (CM6) and southern (CM2) line, (b) comparison of average, low-frequency kinetic energy per sensor. Solid bars represent northern line and dashed southern line. The low-frequency energy is estimated as in Fig. 9.

southern line. The low-frequency kinetic energy $(\bar{\Phi}_{uu}+\bar{\Phi}_{vv})$ is estimated as in Fig. 9.

b. Coherence and phase

The most energetic low-frequency oscillations at the southern mooring line were found to be coherent horizontally, vertically, and for different measurements at the same meter. For seven data blocks ($K=7$) the level of significant coherence at 95% confidence is estimated (after Benignus, 1969) at 0.67 for the first four bands and drops to 0.40 at $\sigma=0.0772$ cph. In addition, phase errors may be estimated from the standard deviation of the cospectrum and quadrature spectrum among the blocks of data analyzed (see Dobson *et al.*, 1974). For diagrams in this section, the absence of a phase estimate at some frequencies signifies that the standard deviations of the cross-spectral components exceeded their mean values.

Fig. 11 shows the coherence and phase between downstream and cross-stream velocity fluctuations at individual meters on the southern line for frequencies <0.08 cph. In Fig. 11a the results for CM2 reveal coherences in excess of 0.8 at a frequency of 0.0231 cph corresponding to the peaks in the velocity spectra. The phase at this frequency approaches 90° as the phase error bands tighten. Superimposed on this diagram are two overlapping bands indicating the range of frequencies for unstable baroclinic waves. The outer (lightly shaded) band includes all unstable frequencies for the parameters given in Table 1, while the inner (darker) band depicts the range of instabilities with maximum growth rate. According to expressions in (3.13), the phase relationship between lower layer velocity components for a mode 1 wave depends on the sign of $\sin(\pi y/L)$ and is equal to $-\pi/2$ on the shallow side of the channel. Thus, the velocity components at CM2 are coherent at frequencies corresponding to model instabilities and in quadrature with the proper sense for the observations on the upslope side of the overflow.

In Fig. 11b, similar results are displayed for the bottom meters on moorings CM1, CM3 and CM4. Notice that the phase estimates at CM1 are again near $-90°$, as expected. However, the coherence at CM3 is not significant and the phase estimates are erratic. This might be expected near the core of the overflow where the downstream perturbation velocity passes through zero according to the model. At CM4, the coherence rises again and there is one positive phase estimate at $\sigma=0.0151$ cph. However, the temperature record from this meter shows that it was in the warm Atlantic

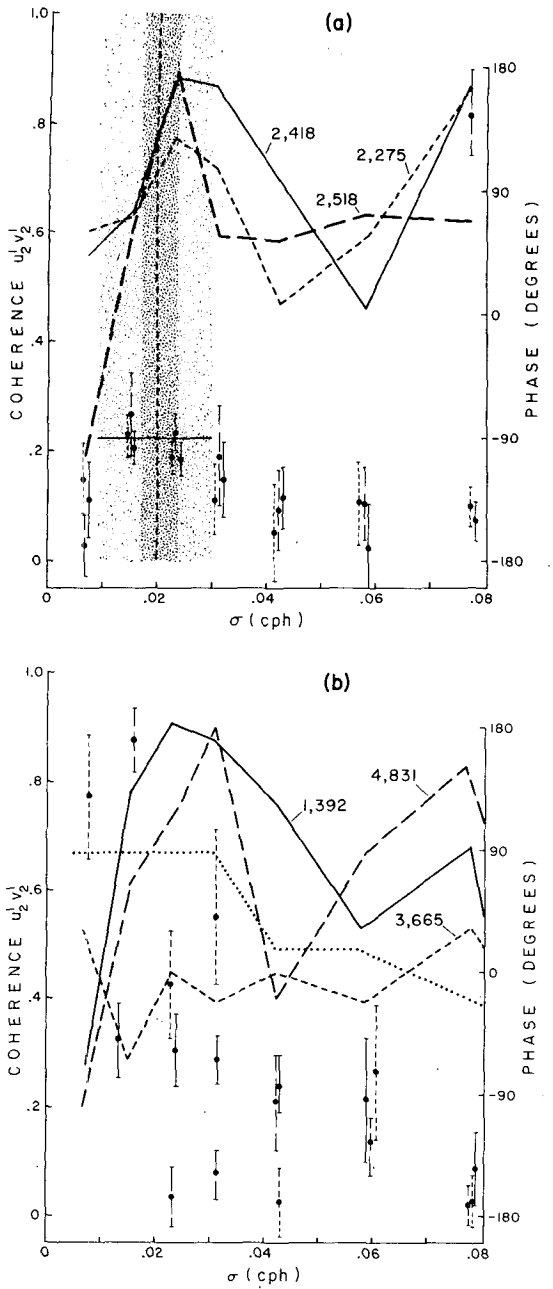

FIG. 11. Coherence and phase between velocity components: (a) CM2 meters [Shaded bands indicate total range of instability frequencies (light) and range of maximal instabilities (dark). Horizontal bar indicates theoretical phase relation (−90°).] and (b) bottom meters on CM1, CM3 and CM4. [The 95% confidence level for coherence with $K=7$ (after Benignus, 1969) is shown by the dotted line.]

water ($T>4$°C) for 32.7% of the time [as compared to 0.4% and 2.3% at CM2 and CM3, respectively (Ross, 1974)] and this may have strongly influenced the sample phases.

The coherence and phase between cross-stream velocity and negative temperature perturbations corresponding to *positive* lower layer thickness anomalies are presented in Fig. 12. Very high coherences (>0.9) are again found for low frequencies at all sensors on CM2 in Fig. 12a where the frequency bands and phase envelope corresponding to model instabilities are again superimposed. The highest coherences are found at the band of maximum growth rate and the corresponding phase estimates for all depths fall near the theoretical

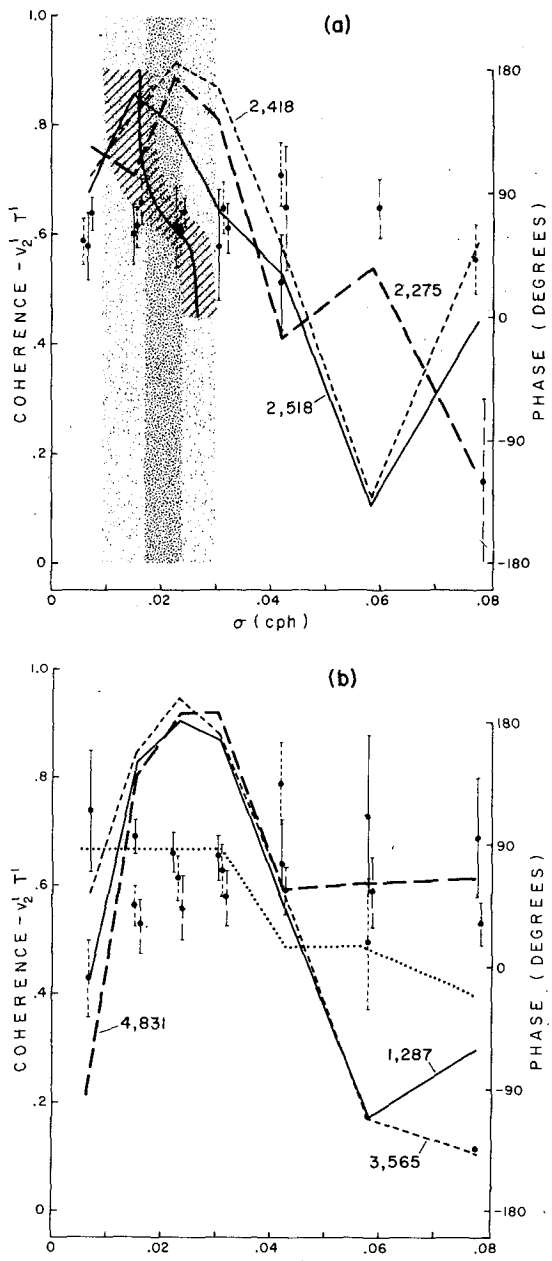

FIG. 12. Negative cross-stream perturbation heat flux: (a) CM2 meters [Instability frequencies are shaded as in Fig. 11a. Cross hatching about solid curve indicates theoretical phase envelope.] and (b) meters near interface on CM1, CM3 and CM4. [The 95% confidence level for coherence ($K=7$) is shown by the dotted line.]

phase envelope. Fig. 12b shows that similar patterns occur 100 m off bottom on CM1 and CM3 and at the bottom on CM4. Notice that coherence estimates in the frequency range for unstable baroclinic waves are consistently above the 95% level of significance.

A summary of the negative perturbation heat flux at the southern mooring line is displayed in Fig. 13. The components of negative heat flux vector at low frequencies are obtained by summing the contributions to $-\overline{u'T'}$ and $-\overline{v'T'}$ from the first four frequency bands ($0<\sigma\leqslant 0.0310$ cph) in the spectrum. The resulting vector, resolved at 250T, lies consistently to the right of the mean velocity which is also plotted. Thus at every meter in the southern line there is a net component of negative perturbation heat flux across the stream which is represented by the local mean velocities. This transfer is most intense at the interface between the overflow and warm Atlantic water and is consistent with the conversion of mean available potential energy of the sloping isotherms into the perturbation fields.

The coherence and phases between cross-stream velocity components at the base of separate moorings in the southern line is shown in Fig. 14. The peak coherence at low frequencies is greatest (~0.95) between adjacent moorings and the corresponding phase estimates are roughly −30°. When the moorings are separated by one, the peak coherence drops to about 0.85 and the phase estimates lie between −60° and −80°. With an average separation of 15 km between moorings, these phase differences are consistent with the propagation of an *untilted* 80 km model wave at an angle of 27° to the right of the normal to the section line or at

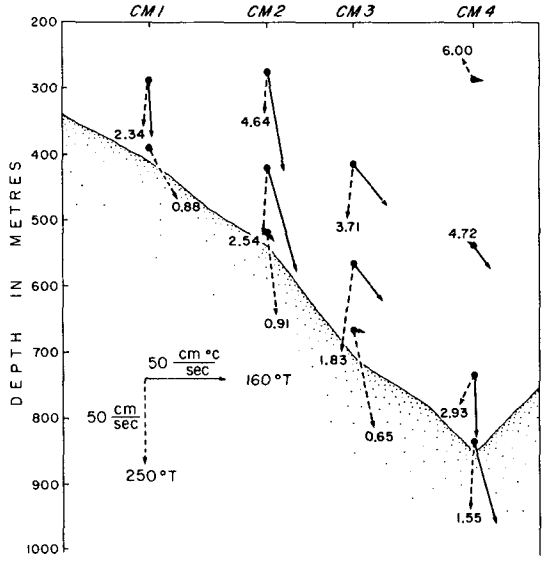

FIG. 13. Negative perturbation heat flux and average velocity vectors at southern mooring line for the negative perturbation heat flux ($-\overline{u'T'}$, $-\overline{v'T'}$) [solid lines], and the average velocity ($\bar{u},\bar{v}$) [dashed lines]. Numerals at tips of velocity vectors indicate average temperatures over record.

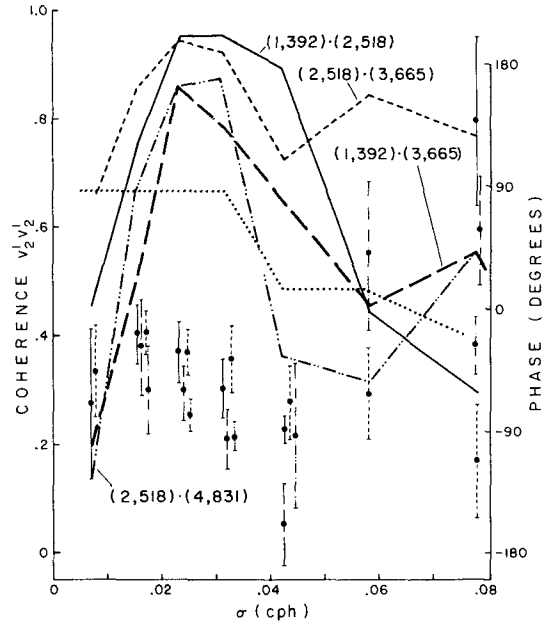

FIG. 14. Cross-stream coherence and phase between cross-stream velocities at bottom meters. The 95% confidence level for coherence ($K=7$) is shown by the dotted line.

240T. Notice from Fig. 5 that this is very nearly the direction of the mean velocity at the bottom meter.

An attempt was made to measure the phase shift between the cross-stream perturbation velocities in the upper and lower layers by correlating the records from the bottom and top meter on each mooring. These results are displayed in Fig. 15 along with the frequency range and predicted phases for the channel flow instabilities. At moorings CM1, CM2 and CM3, the vertical coherence is very high in the instability frequency band, but at CM4 the coherence is insignificant. This is due to the fact that the records from (4,286) were unusually short ($K=3$) so the level of significance was higher (0.92 at the lowest frequencies) than shown on the figure. According to the channel flow model, the phase difference between upper and lower layer velocities approaches zero on the marginal stability curve and dips to −40° near the maximum instability. The phase differences from the overflow records, however, appear to be slightly positive but not essentially different from zero in the frequency band for instabilities. For moorings CM1–CM3 the interpretation of these results as phase shifts between layers may be at fault since it is clear from the temperature records and progressive vector diagrams of Fig. 5 that meter (3,415), for example, is in the overflow for a large portion of the time. The same is true for (1,287) and (2,275). On the other hand, (4,286), with a mean temperature of 6°C, was in the upper layer for a high percentage of the record, but its shortness and low coherence limit its applicability as an upper layer record. Furthermore (4,831) was not in the overflow water for the entire record.

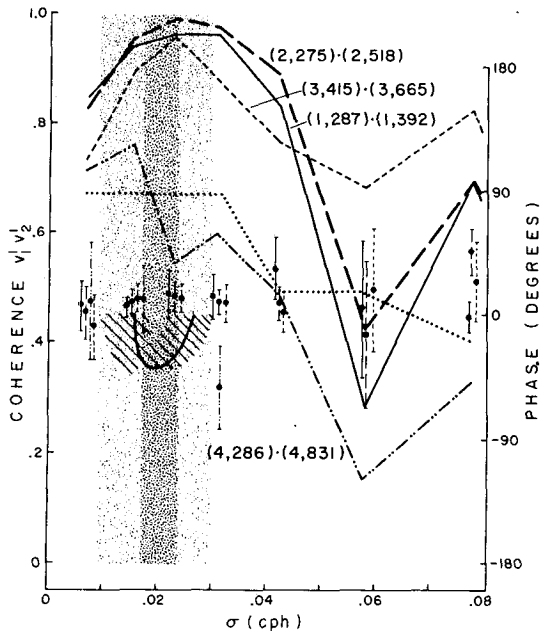

FIG. 15. Vertical coherence and phase between cross-stream velocities at top and bottom meters on southern mooring line. Instability frequencies are shaded as in Fig. 9 and cross-hatching depicts theoretical phase envelope. The 95% confidence level for coherence ($K=7$) is shown by the dotted line.

Hence it is not possible to measure the phase relationship between the two layers from these data.

Finally, the upstream coherence between cross-stream velocities at the base of moorings CM1, CM2 and CM6 are presented in Fig. 16. The peak coherence (0.45) occurs at an instability frequency $\sigma=0.0231$ cph, but is not significant at the 95% confidence level. Furthermore, the phase differences show no particular trend with frequency although the pattern for each correlation is the same. No other correlations between records on the northern and southern lines exhibit higher coherence in the frequency range for unstable baroclinic waves.

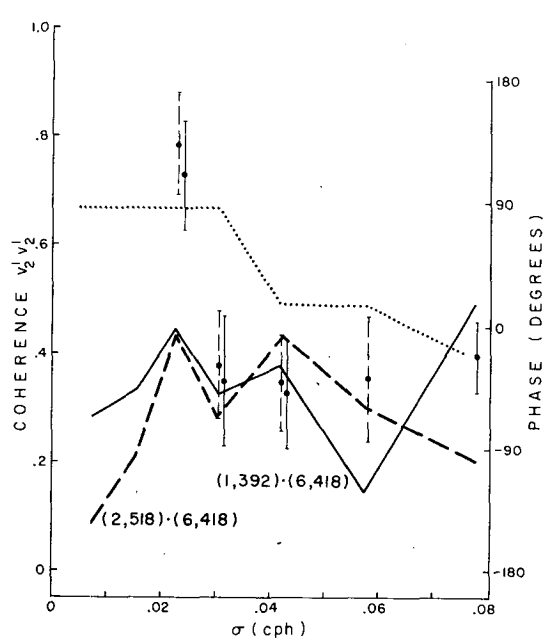

FIG. 16. Coherence and phase between cross-stream velocities at bottom on southern (CM1, CM2) and northern (CM6) mooring lines. The 95% confidence level for coherence ($K=7$) is shown by the dotted line.

5. Conclusions

In summary, the overflow of Norwegian Sea water through the Denmark Strait has been modeled as a uniform, geostrophic bottom current in a straight channel, and properties of the observed low-frequency variability have been compared to those of the linear unstable baroclinic waves which the system admits. Oscillations in the unstable frequency bands are found to be very energetic and highly coherent. The lower layer velocity components are nearly in quadrature and there is a distinct cross-stream component of the perturbation heat flux signifying the transformation of mean potential energy associated with the sloping isotherms into the perturbations. Furthermore, cross-stream phase lags are consistent with the detection of the most unstable model wave propagating in the direction of the mean flow.

Despite the success of the linear model, several aspects of the model and data indicate that the limits of its applicability may have been exceeded. Pedlosky (1972) has shown that packets of unstable baroclinic waves travel at the group speed defined by

$$c_g=\frac{d(kc)}{dk}=c_r+\frac{2(\alpha F-m^2\pi^2)}{F}\frac{dc_r}{d\alpha}. \tag{5.1}$$

This quantity, easily computed from the numerical solutions to the dispersion relation, has a value of 18 cm s^{-1} for the maximally unstable model wave indicated in Fig. 7. Using the corresponding growth rate ($\sigma_i=1.98\times10^{-5}$ s^{-1}), a simple calculation gives the downstream e-folding scale for a perturbation

$$x_e=c_g/\sigma_i=9.1 \text{ km}. \tag{5.2}$$

Hence the downstream extent of the linear regime is an order of magnitude smaller than the distance between the northern and southern lines (~150 km). Furthermore, there is evidence of strong nonlinearity in the observations. For example, the 200 m difference in the overflow layer depth illustrated in Fig. 4 would be difficult to identify as a weak oscillation of the interface.

Although a rigorous treatment of finite-amplitude effects is beyond the scope of the present investigation, several inconsistencies between the linear model and experimental results may be rationalized by reference to Pedlosky's (1970) analytical treatment of a similar two-layer inviscid model. In Pedlosky's case the layers are of equal depth and the gradient in planetary vor-

ticity (β-effect) rather than the bottom slope provides the restoring force for wave motions. His solution for the nonlinear growth of a uniform infinitesimal perturbation exhibits a limit cycle behavior (vacillation) in which the amplitude of the unstable waves grows to a maximum and decays periodically. Similarly, a spatial modulation in amplitude occurs if the flow is perturbed at a single location. In general, modulations in both space and time are possible and the resulting wave packet solutions resemble those for solitary waves.

From another standpoint, recent laboratory experiments with two-layer jets on a slope in a rotating system (Smith, 1975) have demonstrated that finite-amplitude baroclinic instabilities in a steady source flow may take the form of a train of discrete vortices which propagate in the downstream direction. Although a link between laboratory and theoretical finite-amplitude results has not yet been established, either effect would appear as amplitude oscillation to a fixed observer and could explain the high degree of intermittency found in the current meter records at low frequencies. In addition, according to Pedlosky's results, the phase relationship between the two layers depends on the rate of change of the amplitude of the unstable wave. If the amplitude oscillates, the net effect over several cycles may be zero phase shift between upper and lower layers which would be consistent with the results of Fig. 15. Moreover, the formation of a discrete vortex would lead to stronger downstream wave velocities than are present in the linear wave and would produce a more even partitioning of perturbation kinetic energy as indicated in Fig. 9. Finally, the loss of significant coherence from the northern to the southern mooring line in the Denmark Strait could result from nonlinear interactions within the baroclinic wave field and/or the generation of new instabilities along the channel.

Present efforts are directed toward a detailed examination of the nonlinear aspects of the overflow variability in an attempt to give quantitative support to the above suggestions. The hope is to provide a deeper insight into the inherent sources of low-frequency oscillations in the Denmark Strait overflow and similar bottom currents.

Acknowledgments. The author is grateful to the members of the Ocean Circulation Division at the Bedford Institute of Oceanography for their helpful suggestions throughout this investigation and particularly to C. K. Ross and Dr. G. T. Needler for many useful discussions. This work was carried out under a postdoctoral fellowship from the National Research Council of Canada.

APPENDIX

Derivation of Stability Equations and Associated Energy Transformations

1. Stability equations

The linear stability problem for a two-layer channel flow on a beta-plane is outlined below. The formulation closely parallels that of Pedlosky (1970) and the reader is referred to his paper for further discussion. The basic flow field is sketched in Fig. 6. The velocity U_i $(i=1, 2)$ in each layer is uniform, the mean layer depths are D_i $(i=1, 2)$, and the channel walls are at $y=\pm L/2$. The upper surface at $z=D_1+D_2$ is a stress-free rigid lid, the interface is at $z=D_2+\phi(x,y,t)$, and the sloping channel floor is at $z=sy$, where $s=\tan\alpha$. The dimensionless variables (primed) are defined as follows:

$$\left.\begin{aligned}
(u_i,v_i,w_i)&=U_2(u_i',v_i',\delta w_i'), \quad \delta=\frac{D_2}{L}\\
(x,y,z)&=L(x',y',\delta z')\\
P_1&=\rho_1 g(D_1+D_2-z)+\rho_1 U_2 fLp_1'\\
P_2&=\rho_1 g(D_1+D_2-z)+\rho_2 g_r(D_2-z)+\rho_2 U_2 fLp_2',\\
g_r&=\frac{\Delta\rho}{\rho_2}g\\
t&=L/U_2 t'\\
\phi&=d\phi', \quad d=\frac{fLU_2}{g_r}
\end{aligned}\right\} \tag{A1}$$

Then using the Boussinesq approximation and assuming δ and the Ekman number are small, the scaled equations of motion may be written as (dropping primes)

$$u_{ix}+v_{iy}+w_{iz}=0, \tag{A2}$$

$$\epsilon(u_{it}+\mathbf{u}_i\cdot\nabla u_i)-(1+\epsilon \mathrm{F}\beta y)v_i=-p_{ix}+\frac{\mathrm{E}}{2}u_{izz}, \tag{A3}$$

$$\epsilon(v_{it}+\mathbf{u}_i\cdot\nabla v_i)+(1+\epsilon \mathrm{F}\beta y)u_i=-p_{iy}+\frac{\mathrm{E}}{2}v_{izz}, \tag{A4}$$

$$0=-p_{iz} \quad (i=1, 2), \tag{A5}$$

with boundary conditions

$$1. \quad w_1=p_1=0 \quad \text{at} \quad z=\frac{\gamma+1}{\gamma}, \tag{A6}$$

$$\left.\begin{aligned}
2. \quad & w_i=\epsilon \mathrm{F}(\phi_t+u_i\phi_x+v_i\phi_y) \quad (i=1, 2)\\
& p_2=p_1+\phi
\end{aligned}\right\} \quad \text{at} \quad z=1+\epsilon \mathrm{F}\phi, \tag{A7}$$

3. $w_2=-\epsilon \mathrm{F} B v_2+\epsilon r(v_{2x}-u_{2y})$ at $z=-\epsilon \mathrm{F} B y$, (A8)

4. $v_i=0 \quad (i-1, 2)$

$$\lim_{x\to\infty}\frac{1}{2x}\int_{-x}^{x} u_{i_t}\Big|_{y=-\frac{1}{2}}^{y=\frac{1}{2}} dx=0 \Bigg\} \text{ at } y=\pm\tfrac{1}{2}, \quad \text{(A9)}$$

where

$$\left.\begin{aligned}
&\epsilon=\frac{U_2}{fL} && \text{(Rossby number)}\\
&\beta=\frac{g_r D_2}{fU_2}\left(\frac{\cot\theta}{R}\right)_y && \text{(beta effect, } R=\text{earth radius, } \theta=\text{latitude)}\\
&\mathrm{E}=\frac{\nu}{fD_2{}^2} && \text{(Ekman number)}\\
&\mathrm{F}=\frac{f^2L^2}{f_r D_2} && \text{(internal Froude number)}\\
&\gamma=\frac{D_2}{D_1} && \text{(layer depth ratio)}\\
&\mathrm{B}=\frac{g_r s}{fU_2} && \text{(bottom slope parameter)}\\
&r=\mathrm{E}^{\frac{1}{2}}/2\epsilon && \text{(friction parameter)}
\end{aligned}\right\}. \quad \text{(A10)}$$

Notice that the vertical velocity at the bottom has both a topographic component and a viscous component resulting from Ekman suction. Also, note that the value of β should not reflect the full variation of the Coriolis parameter with latitude (θ) but only its projection on the y axis.

For the case $r\leqslant 1$, the variables may be expanded in powers of ϵ. At lowest order the flow is geostrophic while at first order the vertically integrated vorticity equations yield two coupled equations for the reduced pressures p_i:

$$\gamma^{-1}\left(\frac{\partial}{\partial t}-p_{1_y}\frac{\partial}{\partial x}+p_{1_x}\frac{\partial}{\partial y}\right)[\nabla^2 p_1+\mathrm{F}\beta y]=-w_i, \quad \text{(A11)}$$

$$\left(\frac{\partial}{\partial t}-p_{2_y}\frac{\partial}{\partial x}+p_{2_x}\frac{\partial}{\partial y}\right)[\nabla^2 p_1+\mathrm{F}(\beta-\mathrm{B})y] =w_i-r\nabla^2 p_2, \quad \text{(A12)}$$

where

$$w_i=\mathrm{F}\left(\frac{\partial}{\partial t}-p_{2_y}\frac{\partial}{\partial x}+p_{2_x}\frac{\partial}{\partial y}\right)(p_2-p_1). \quad \text{(A13)}$$

The pressures p_i may then be decomposed into a mean field plus a perturbation, i.e.,

$$p_i(x,y,t)=-U_i y+\psi_i(x,y,t), \quad \text{(A14)}$$

where $U_2\equiv 1$. The resulting equations for the perturbation pressures are

$$\left(\frac{\partial}{\partial t}+U_1\frac{\partial}{\partial x}\right)[\nabla^2\psi_1+\gamma\mathrm{F}(\psi_2-\psi_1)] +\mathrm{F}[\beta+\gamma(1-U_1)]\psi_{1x}=0, \quad \text{(A15)}$$

$$\left(\frac{\partial}{\partial t}+\frac{\partial}{\partial x}\right)[\nabla^2\psi_1-\mathrm{F}(\psi_2-\psi_1)] +\mathrm{F}[\beta-\mathrm{B}+(1-U_1)]\psi_{2x}=-r\nabla^2\psi_2. \quad \text{(A16)}$$

The appropriate lateral boundary conditions at $y=\pm\frac{1}{2}$ are

$$\frac{\partial\psi_i}{dx}=0, \quad \text{(A17)}$$

$$\lim_{x\to\infty}\frac{1}{2x}\int_{-x}^{x}\psi_{i_{yt}}\Big|_{y=-\frac{1}{2}}^{y=\frac{1}{2}} dx=0. \quad \text{(A18)}$$

2. Energy transformations

In order to identify all possible energy sources for the perturbations, the energy transformations will be derived for a general two-layer flow with horizontal shear in each layer. The analysis essentially follows that of Smith (1974).

We define downstream and areal averages as

$$\langle(\ )\rangle=\frac{k}{2\pi}\int_0^{2\pi/k}(\ )dx; \quad \overline{(\ )}=\int_{-\frac{1}{2}}^{\frac{1}{2}}\langle(\ )\rangle dy. \quad \text{(A19)}$$

Because energy transformation occur at second order, a more complete definition of the mean flow than in (A14) is required to include time-varying second order modifications, i.e.,

$$p_i(x,y,t)=\Psi_i(y,t)+\psi_i(x,y,t), \quad \text{(A20)}$$

where

$$\Psi_i(y,t)=<p_i(x,y,t)>.$$

Notice that ψ_i and its derivatives are periodic in x with wavelength $2\pi/k$.

Expressions for the average kinetic energy $\bar{K}$ and available potential energy $\bar{P}$ of the mean flow are then

$$\left.\begin{aligned}
\bar{K}&=\tfrac{1}{2}(\gamma^{-1}\overline{\Psi_{1_y}^2}+\overline{\Psi_{2_y}^2})\\
\bar{P}&=\frac{\mathrm{F}}{2}\overline{(\Psi_2-\Psi_1)^2}
\end{aligned}\right\}, \quad \text{(A21)}$$

whereas the perturbation kinetic K' and available potential P' energies are given by

$$\left.\begin{aligned}
K'&=\frac{\gamma^{-1}}{2}\overline{(\psi_{1x}{}^2+\psi_{1_y}{}^2)}+\tfrac{1}{2}\overline{(\psi_{2x}{}^2+\psi_{2_y}{}^2)}\\
P'&=\frac{\mathrm{F}}{2}\overline{(\psi_2-\psi_1)^2}
\end{aligned}\right\}. \quad \text{(A22)}$$

Equations for the time rate of change of these quantities are produced by computing

$$\overline{\Psi_1\cdot(\text{A11})+\Psi_2\cdot(\text{A12})},\ \overline{(\Psi_2-\Psi_1)\cdot(\text{A13})},$$
$$\overline{\psi_1\cdot(\text{A11})+\psi_2\cdot(\text{A12})},\ \text{and}\ \overline{(\psi_2-\psi_1)(\text{A13})}.$$

The result may be expressed in concise form as

$$\frac{\partial\bar{K}}{\partial t}=\{K',\bar{K}\}-\{\bar{K},\bar{P}\}+\{\text{bottom},\bar{K}\}, \tag{A23}$$

$$\frac{\partial\bar{P}}{\partial t}=\{\bar{K},\bar{P}\}-\{\bar{P},P'\}, \tag{A24}$$

$$\frac{\partial K'}{\partial t}=\{P',K'\}-\{K',\bar{K}\}-\{K',\text{dissipation}\}, \tag{A25}$$

$$\frac{\partial P'}{\partial t}=\{\bar{P},P'\}-\{P',K'\}, \tag{A26}$$

where the boundary conditions (A9) have been used and the forms have been made symmetric (leaving the balance unchanged) by adding and subtracting the quantities $[1-1/(2\gamma)]\Psi_1\langle w_i\rangle$ and $[1-1/(2\gamma)]\Psi_1 w_i$ from the expressions for $\{\bar{K},\bar{P}\}$ and $\{K',P'\}$, respectively. The transfer terms appearing in (A23)–(A26) are defined by

$$\left.\begin{aligned}
\{K',\bar{K}\}&=\overline{\gamma^{-1}\psi_{1x}\psi_{1y}\Psi_{1yy}}\quad\overline{\psi_{2x}\psi_{2y}\Psi_{2yy}}\\
\{\bar{K},\bar{P}\}&=\left(\Psi_2-\frac{\gamma+1}{2\gamma}\Psi_1\right)\langle w_i\rangle\\
\{\bar{P},P'\}&=\mathrm{F}\overline{(\Psi_2-\Psi_1)_y\psi_{2x}(\psi_1-\psi_2)}\\
\{P',K'\}&=\overline{\left(\psi_2-\frac{\gamma+1}{2\gamma}\psi_1\right)w_i}\\
\{\text{bottom},\bar{K}\}&=r\overline{\Psi_2\Psi_{2yy}}\\
\{K',\text{dissipation}\}&=-\overline{r\psi_{2x}{}^2+\psi_{2y}{}^2}+r\langle\psi_2\psi_{2y}\rangle\Big|_{y=-\frac{1}{2}}^{y=\frac{1}{2}}
\end{aligned}\right\}. \tag{A28}$$

The interpretation of these terms is discussed by Smith (1974). They identify the sources, sinks and transformations of energy which are possible in the shearing two-layer model.

The energy equation for the perturbations alone may be obtained by combining (A25) and (A26) to give

$$\frac{\partial}{\partial t}(K'+P')=\{\bar{P},P'\}-\{K',\bar{K}\}-\{K',\text{dissipation}\}. \tag{A29}$$

REFERENCES

Benignus, V. A., 1969: Estimation of the coherence spectrum and its confidence interval using the fast Fourier transform. *IEEE Trans. Audio Electroacoustics*, **AU-17**, 145–150.

Blumsack, S. L., and P. J. Gierasch, 1972: Mars: The effects of topography on baroclinic instability. *J. Atmos. Sci.*, **29**, 1081–1089.

Cooper, L. N. H., 1955: Deep water movements in the North Atlantic as a link between climatic changes around Iceland and biological productivity of the English Channel and Celtic Sea. *J. Marine Res.*, **14**, 347–362.

Dobson, F., R. F. Brown and D. R. Chang, 1974: A set of programs for analysis of time series data including fast Fourier transform spectral analysis. Rept. BI-C-74-2, Bedford Institute of Oceanography, Dartmouth, Nova Scotia.

Hart, J. E., 1974: On the mixed stability problem for quasi-geostrophic ocean currents. *J. Phys. Oceanogr.*, **4**, 349–356.

Harvey, J. G., 1961: Overflow of cold deep water across the Iceland-Greenland Ridge. *Nature*, **189**, 911–913.

Lee, A. J., and D. Ellett, 1967: On water masses of the northwest Atlantic Ocean. *Deep-Sea Res.*, **14**, 183–190.

Mann, C. R., 1969: Temperature and salinity characteristics of the Denmark Strait overflow. *Deep-Sea Res.*, **16**, Suppl., 125–137.

Munk, W. H., F. F. Snodgrass and M. J. Tucker, 1959: Spectra of low-frequency ocean waves. *Bull. Scripps Inst. Oceanogr.*, **7**, 283–362.

Orlanski, I., 1969: The influence of bottom topography on the stability of jets in a baroclinic fluid. *J. Atmos. Sci.*, **26**, 1216–1232.

Pedlosky, J., 1964: The stability of currents in the atmosphere and the ocean. Part 1. *J. Atmos. Sci.*, **21**, 201–219.

——, 1970: Finite-amplitude baroclinic waves. *J. Atmos. Sci.*, **27**, 15–30.

——, 1972: Finite-amplitude baroclinic wave packets. *J. Atmos. Sci.*, **29**, 680–686.

Ross, C. K., 1974: Preliminary results of recent overflow measurements in Denmark Strait. Presented at SCOR/SCAR Polar Oceans Conference, Montreal, Canada.

Smith, P. C., 1973: The dynamics of bottom boundary currents in the ocean. Ph.D. thesis, MIT.

——, 1975: Experiments with viscous source flows in rotating systems. (Submitted to *Geophys. Fluid Dyn.*)

Smith, R. K., 1974: On limit cycles and vacillating baroclinic waves. *J. Atmos. Sci.*, **31**, 2008–2011.

Worthington, L. V., 1969: An attempt to measure the volume transport of Norwegian Sea overflow water through the Denmark Strait. *Deep-Sea Res.*, **16**, Suppl., 421–432.